Applied Catalysis B: Environmental 170-171 (2015) 206–214

Contents lists available at ScienceDirect

Applied Catalysis B: Environmental

journal homepage: www.elsevier.com/locate/apcatb

Hierarchically Z-scheme photocatalyst of Ag@AgCl decorated on $BiVO_4$ (0 4 0) with enhancing photoelectrochemical and photocatalytic performance

Hongyan Li[a,c], Yingjuan Sun[b,c], Bin Cai[d], Shiyu Gan[a], Dongxue Han[a,*], Li Niu[a], Tongshun Wu[a,*]

[a] State Key Laboratory of Electroanalytical Chemistry, c/o Engineering Laboratory for Modern Analytical Techniques, Changchun Institute of Applied Chemistry, Chinese Academy of Sciences, Changchun, 130022 Jilin, China
[b] State Key Laboratory of Polymer Physics and Chemistry, Changchun Institute of Applied Chemistry, Chinese Academy of Sciences, Changchun, 130022 Jilin, China
[c] University of Chinese Academy of Sciences, Beijing 100049, China
[d] Physical Chemistry, Technische Universität Dresden, Bergstrasse 66b, 01062 Dresden, Germany

ARTICLE INFO

Article history:
Received 26 November 2014
Received in revised form 26 January 2015
Accepted 31 January 2015
Available online 2 February 2015

Keywords:
$BiVO_4$
AgCl
Photocatalytic
Photoelectrochemical
Z-scheme

ABSTRACT

Crystal facet dependence, as the crucial factor for semiconductor photocatalysis, is a significant strategy for optimizing the reactivity of photocatalyst. Given that there is a strong correlation between crystal facet and photocatalytic activity, we herein designed the Ag@AgCl core–shell structure decorated on (0 4 0) crystal facet of $BiVO_4$ (Ag@AgCl/$BiVO_4$) as a hierarchical Z-scheme photocatalytic system by a simple route. In this hybridization system, the metallic Ag species not only act as the solid-state electron mediator, but can also absorb the photons from incident light and present the SPR-effect. As expected, such Ag@AgCl/$BiVO_4$ heterostructure exhibits highly efficient photocatalytic performance and the first-order kinetic constant of photodegradation of Rhodamine B (RhB) is 300 times of pristine $BiVO_4$. Moreover, by means of the EIS, LSV and I-t measurements, the Ag@AgCl/$BiVO_4$ heterostructure also presents extraordinary photoelectrochemical performance. Focus is then given toward a novel perspective for understanding the mechanism of interfacial charge transfer of photocatalytic on the basis of the $BiVO_4$-based all-solid-state Z-scheme photocatalyst. This work is expected to open up new insights into the architectural design of novel Z-scheme photocatalysts with high photoactivity and further utilization in the field of environmental or energy.

1. Introduction

With unceasingly expanding industrial development after industrial revolution, the environmental pollution caused by industrial effluent as well as toxic air contaminants has become an overwhelming problem all over the world [1,2]. Hence, it is imminent to solve the current environmental crises facing the modern society. Coincidentally, semiconductor-based photocatalytic and photoelectrochemical have recently been developed due to its potential applications in coping with the environmental pollution and deterioration issues [3–5]. By this token, the construction of efficient semiconductor photocatalyst with high quantum yields and wide-range visible light utilization is the key research emphasis for many researchers [6]. However, pursuing highly efficient visible light driven and charge carriers separation for current photocatalysis system is still a great challenge [4]. In comparison to single-component photocatalyst, the heterostructure photocatalyst usually exhibits a higher photocatalytic performance for the decomposition of various organic contaminants since it can facilitate the photo-induced carriers separation and benefit to suppress recombination of the electron–holes, leaving more charge carriers to form reactive species [7,8].

Over the past years, the designing and investigations on the semiconductor heterostructure photocatalyst mainly include metal-doped, P–N heterojunction and Z-scheme [9–11]. Among the numerous heterojunction photocatalysts, the Z-scheme photocatalytic system has great potential to develop separation of the photo-induced electron and holes of the composition photocatalyst [5]. Thanks to its superb photocatalysis properties and photostabilities, the artificial heterogeneous Z-scheme photocatalytic

* Corresponding authors. Tel.: +86 43185262425; fax: +86 43185262800.
E-mail address: dxhan@ciac.ac.cn (D. Han).

http://dx.doi.org/10.1016/j.apcatb.2015.01.043
0926-3373/

systems overcome the drawbacks of single-component photocatalysts and satisfy those aforementioned requirements [12–14]. Tada et al. firstly constructed an all-solid-state Z-scheme TiO_2–Au–CdS system by means of photochemical deposition–precipitation method which presents higher photocatalytic efficiency [11]. Sekizawa et al. also reported the artificial Z-scheme system for reducing CO_2 which was driven by visible light and used a hybrid of a supramolecular metal complex (the CO_2-reduction photocatalyst) and semiconductor particles (the oxidation photocatalyst for methanol) [12]. Recently, bismuth vanadate ($BiVO_4$), as the star material, is getting more and more attention to construct the Z-scheme photocatalytic system due to its superior performance in photoelectrochemical water oxidation and degradation of pollutants field [15]. For instance, the $BiVO_4$–Ru/$SrTiO_3$:Rh composite was prepared by a liquid–solid state reaction to construct a Z-schemec photocatalytic system for water splitting under visible light irradiation and showed a higher photoactivity than the single component [16]. In addition, the photocatalytic activity of $BiVO_4$ is highly relying on different crystal facet, due to the different charge mobility and energy band levels. Both experimental and theoretical studies demonstrated that the (0 4 0) crystal facets of $BiVO_4$ present high-active for pollutants degradation as well as O_2 evolution which have been reported by Li et al. [17,18]. Xi and Ye also reported that $BiVO_4$ nanoplates with exposed (0 4 0) facets prepared in aqueous ethanolamine solution showed enhanced photocatalytic activity [19]. However, to date, still very few works have been reported on synthesis of the Z-scheme photocatalyst on the highly activity (0 4 0) crystal facet of $BiVO_4$ with well-defined morphology and excellent performance *via* a facile and effective approach. In this case, according to our previous investigation, AgCl-based plasmonic photocatalysis materials have been considered as promising photocatalysts owing to its highly efficient assist photocatalytic activity under visible light irradiation [20,21].

Consequently, in the present study, we for the first time constructed a hierarchical Z-scheme photocatalyst Ag@AgCl/$BiVO_4$ composite, in which Ag@AgCl core–shell structure was decorated on (0 4 0) crystal facet of $BiVO_4$ by means of a simple two-step route. Further, the photocatalytic activity of the Ag@AgCl/$BiVO_4$ heterostructure composite was investigated by a representative model of Rhodamine B (RhB) degradation in the dyestuffs solution under visible light irradiation. It is worth pointing out that the metallic Ag species not only act as the solid state electron mediator, but also can absorb photons from incident light and present SPR-effect in this hybridization system. Detailed mechanism toward the photocatalysis of this Ag@AgCl/$BiVO_4$ heterostructure has been further proposed and discussed. Such distinctive heterogeneous Z-scheme photocatalytic system has greatly overcome the drawbacks of single-component $BiVO_4$ and realized the high charge-separation efficiency, strong redox ability and long-term stability.

2. Experimental

2.1. Chemicals

Bismuth nitrate pentahydrate ($Bi(NO_3)_3{\cdot}5H_2O$, 98%) and ammonium vanadate (NH_4VO_3, 99.0%) were purchased from Afla Aeser and used without further purification. Silver nitrate ($AgNO_3$), ferric chloride ($FeCl_3$) and ammonium oxalate ($(NH_4)_2C_2O_4$) were obtained from Sinopharm Chemical Reagent (Shanghai, China) and used as received. All aqueous solutions were prepared with ultrapure water (>18.2 MΩ cm) from a Milli-Q Plus system (Millipore). All glassware used in the following procedures were cleaned in a bath of freshly prepared 3:1 HCl:HNO_3 (aqua regia) and rinsed thoroughly by ultrapure-water prior to use.

2.2. Preparation of Ag@AgCl/$BiVO_4$ heterostructure

2.2.1. Preparation of $BiVO_4$ sample

$BiVO_4$ sample with dominant exposed (0 4 0) facets was synthesized by a previously reported method [22–24]. Typically, the precursors of $Bi(NO_3)_3{\cdot}5H_2O$ (6 mmol) was dissolved in HNO_3 (1 mol L^{-1}, 32 mL) aqueous solution under ultrasonic processing until a clear solution was formed. Then precursors of NH_4VO_3 (6 mmol) was added to the above solution under vigorously magnetic stirring. Subsequently, $CO(NH_2)_2$ (3.0 g) was added to the solution when the color of the mixture changed to yellowish orange, and the mixture was heated to 80 °C and kept for 24 h. After the resulting precipitate was cooled to room temperature, a vivid yellow power was separated by filtration, washed with ultrapure-water for more than 5 times, and then dried at 60 °C in air for overnight. The product obtained was denoted $BiVO_4$.

2.2.2. Preparation of Ag/$BiVO_4$ sample

$BiVO_4$ (0.50 g) was added to $(NH_4)_2C_2O_4$ (0.8 g L^{-1}, 100 mL) aqueous solution in a 250 mL beaker under ultrasonic processing until a well-distributed dispersion solution formed. Then, $AgNO_3$ (0.05 g) was put into the above dispersion suspension under magnetic stirring. Subsequently, the obtained yellow colored mixture was irradiated by Xenon arc lamp (CHF-XM35-500 W, Beijing Trusttech Co., Ltd., China) light for 30 min. The color of the system turned from vivid yellow to grayish-green, which means the generation of Ag species in the reaction system. The resulting samples were then filtered, washed and dried at 60 °C for 3 h to obtain the Ag/$BiVO_4$ composite. The chemical reaction for the deposition of the Ag component should be formulated as:

$$BiVO_4 + h\nu \rightarrow h^+ + e^-$$

$$Ag^+ + e^- \rightarrow Ag$$

$$C_2O_4^{2-} + h^+ \rightarrow CO_2 + CO_2^-$$

2.2.3. Preparation of Ag@AgCl/$BiVO_4$ sample

The Ag@AgCl/$BiVO_4$ composite was prepared by an in situ oxidation reaction between Ag/$BiVO_4$ and $FeCl_3$ aqueous solution (0.1 mol L^{-1}) in a dark condition. Typically, 0.5 g of the Ag/$BiVO_4$ composite was added to 80 mL of $FeCl_3$ solution under stirring at room temperature. After stirring for 30 min, the dark green color of Ag/$BiVO_4$ sample gradually turned to greenish yellow owing to the formation of white AgCl nanoparticles. Then, the product was filtered and washed with ultrapure-water, and dried at 60 °C for 3 h to obtain Ag@AgCl decorated $BiVO_4$ (0 4 0) composites. The final obtained product was denoted Ag@AgCl/$BiVO_4$ heterostructure photocatalyst.

2.2.4. Photocatalytic activity

The photocatalytic activity investigation was tested using a representive model of the degradation of dye Rhodamine B (RhB). In the whole process, the optical system for photodegradation was followed with a similar structure which is mentioned above and equipped with a UV cutoff filter ($\lambda \geq 420$ nm), and the irradiation height was 15 cm. In a typical procedure, the as-prepared Ag@AgCl/$BiVO_4$ heterostructure photocatalyst (0.1 g) were well dispersed into RhB solution (50 mL, 10 mg L^{-1}) under ultrasonication in a home-made reactor equipped with a cooling water circulator assembled to keep the whole reaction system maintaining at a constant temperature. The suspension was stirred for 30 min in the dark to reach adsorption–desorption equilibrium and then exposed to visible-light irradiation to start the photocatalysis reaction. After the photodegradation experiment was triggered by

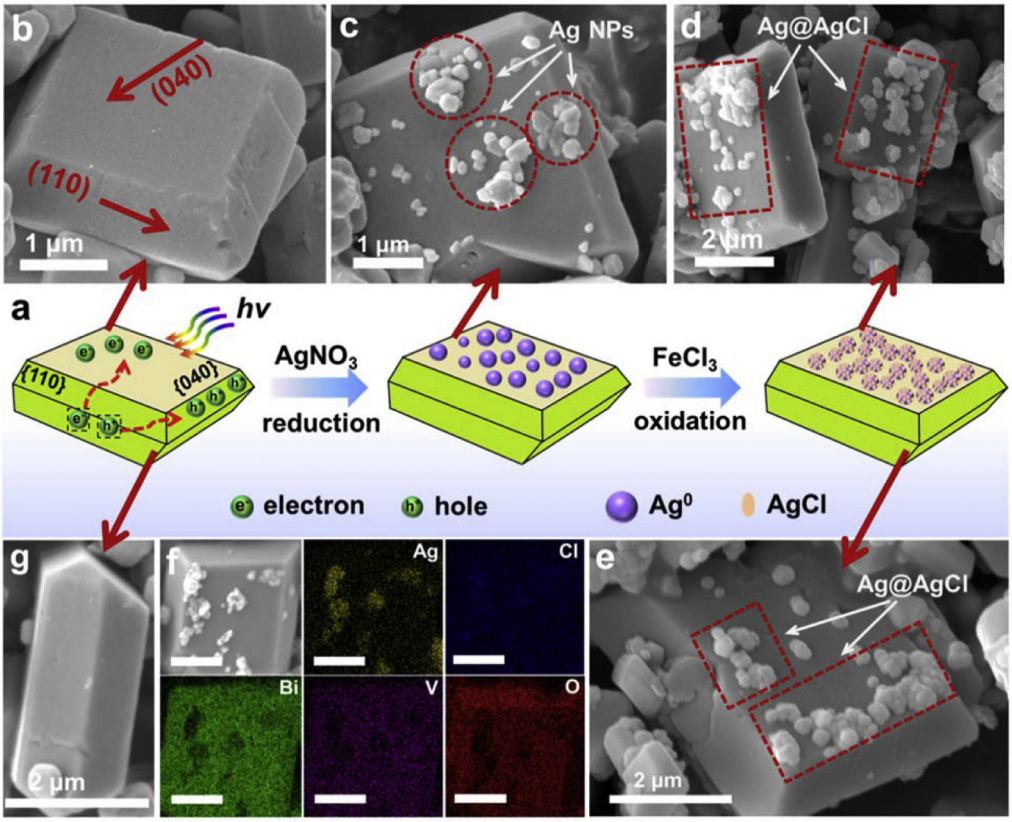

Fig. 1. Synthesis procedure, SEM images and element distribution images of the photocatalysts. (a) Schematic illustration for the formation process of the Ag@AgCl/$BiVO_4$ heterojunction photocatalyst. The typical SEM images of the as-prepared (b) $BiVO_4$, (c) Ag/$BiVO_4$, (d and e) Ag@AgCl/$BiVO_4$ photocatalysts. (f) Element mapping images for Ag, Cl, O, V and Bi in the Ag@AgCl/$BiVO_4$ heterostructure. The scale bar is 2 μm. (g) SEM image of the $BiVO_4$ with exposed (1 1 0) crystal face.

irradiation of visible light, the solution of aliquots volume were periodically withdrawn from the reaction vessel and centrifuged to remove the photocatalyst powders. And the intensity changes of the absorption peak was measured at $\lambda = 552$ nm to determine the concentration of the RhB at different time by using a UV–vis spectrophotometer (ultra-pure water as reference). Normally, C_t is the concentration of RhB solution at time t, C_0 is the initial concentration (10 mg L^{-1}). The photocatalytic measurement mentioned above was repeated twice to ensure the reliability of the results. The reproducibility of the Ag@AgCl/$BiVO_4$ heterostructure was also tested with the following procedure: the photocatalyst was washed with ultra-pure water and ethanol for several times after photoreduction and then retested in the fresh mixture solution of RhB under the same experimental conditions as mentioned above.

3. Results and discussion

3.1. Preparation, electronic images and morphology

Fig. 1a shows the typical schematic illustration for the formation process of the Ag@AgCl/$BiVO_4$ heterojunction photocatalyst. The pristine $BiVO_4$ crystal was obtained through the homogeneous co-precipitation process according to previous reports with some modifications. The SEM images reveal that the morphology of $BiVO_4$ samples exhibit decagonal shape (Fig. 1b and g). Clearly we can observe that these well-defined crystals show smooth surface and relatively sharp edges. Further, those mainly exposed crystal facets of $BiVO_4$ are constituted of two kinds of facets denoted as (0 4 0) and (1 1 0) according to the Li's report [17]. It has been authenticated that these two crystal facets present good charge carriers mobility. Interestingly, the photogenerated electrons and holes tend to accumulate on the (0 4 0) and (1 1 0) facets, respectively, due to their different energy levels in the conduction bands and the valence bands of these facets [17,25]. This phenomenon thereby would make the electrons accumulation facet (0 4 0) and holes accumulation facet (1 1 0) prefer to reduction and oxidation reaction, respectively (Fig. 1a). Under this principle, Ag speices would be photoreduced on the (0 4 0) crystal facet of $BiVO_4$. In the whole photodeposition precess, the $AgNO_3$ was employed as the source of the Ag and the $(NH_4)_2C_2O_4$ as a hole scavenger which can effectively separate the photo-generated electron and hole [26]. As shown in Fig. 1c, it can be clearly seen that Ag NPs deposited well on the (0 4 0) crystal facet, which is well coincided with the theoritical prediction. In order to construct the hierarchical Ag@AgCl/$BiVO_4$ heterostructure, the $FeCl_3$ aqueous solution was introduced to the following reaction. Considering a higher redox potential of Fe^{3+}/Fe^{2+} (+0.771 V *vs.* SHE) than the Ag^+/Ag (+0.223 V *vs.* SHE) [27], the metallic Ag on the surface of $BiVO_4$ can be effectively oxidized by $FeCl_3$ to form the core–shell structure of AgCl enwrapped metallic Ag under mild room-temperature conditions, which is denoted as the Ag@AgCl (Fig. 1d and e). The elemental mapping images (Fig. 1f) could clearly reveal that both the Cl and Ag elements distributed well on the surface of (0 4 0) facet of $BiVO_4$ crystal, which further confirmed the formation of Ag@AgCl/$BiVO_4$ hierarchical structure obtained in this system. The SEM-EDX analysis of the as-prepared $BiVO_4$, Ag/$BiVO_4$ and Ag@AgCl/$BiVO_4$ materials are shown in Fig. S1 (in Supporting information).

3.2. Crystal phase, photophysical properties and compositions

The crystallographic structure of all the as-prepared photocatalyst samples was determined by means of X-ray diffraction (XRD)

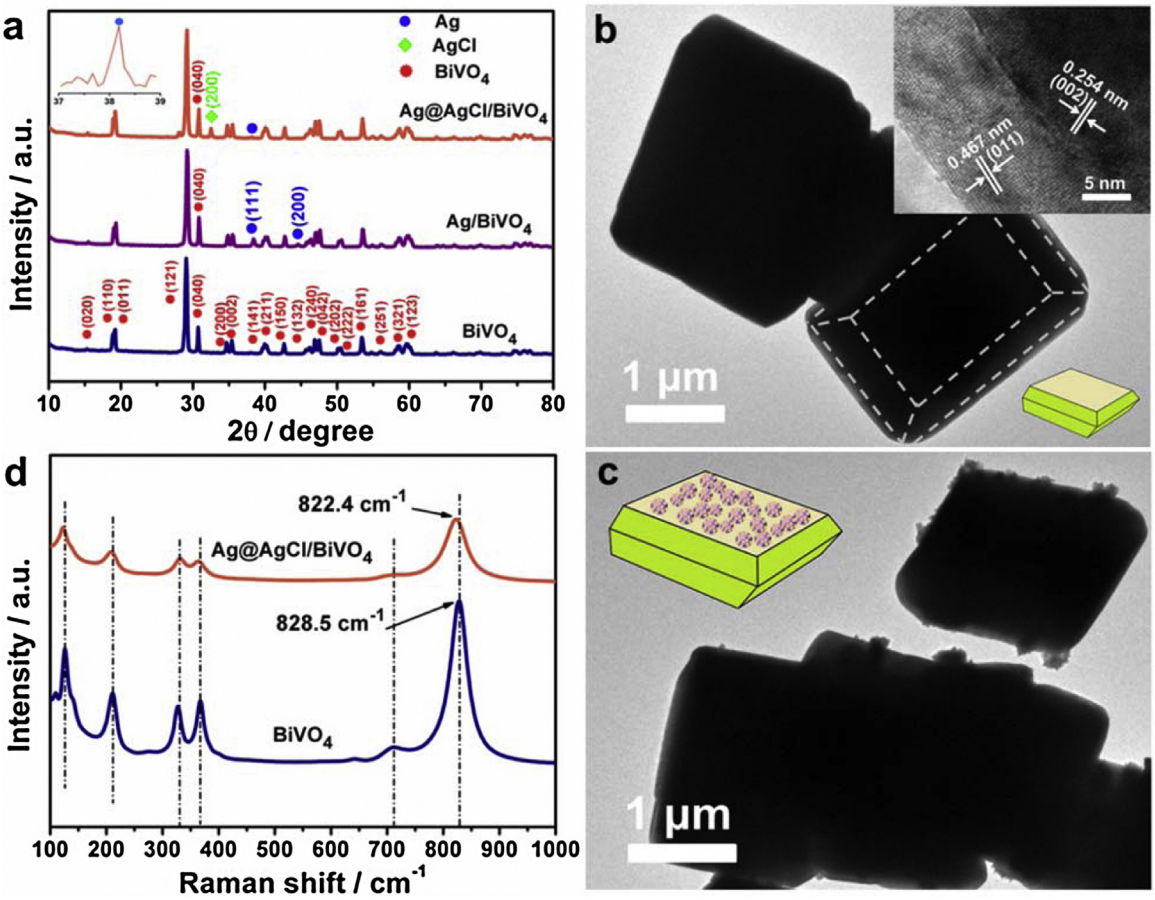

Fig. 2. XRD and TEM characterizations of all photocatalyst samples. (a) XRD patterns of the $BiVO_4$, $Ag/BiVO_4$ and $Ag@AgCl/BiVO_4$. Inset: enlarged XRD pattern at peak position of Ag (1 1 1) of $Ag@AgCl/BiVO_4$. Typical TEM images of (b) $BiVO_4$ inset: HRTEM image of the $BiVO_4$ (c) $Ag@AgCl/BiVO_4$. (d) Raman spectra of $Ag/BiVO_4$ and $Ag@AgCl/BiVO_4$.

analysis (Fig. 2a). The sharp peak patterns of $BiVO_4$ powder sample are well matched with the standard Joint Committee on Powder Diffraction Standards (JCPDS) card No. 14-0688, which is assigned to monoclinic scheelite $BiVO_4$ [23,28]. Additionally, as shown in Fig. 2a, the diffraction peaks (2θ) at 38.1° and 44.3° were found in the $Ag/BiVO_4$, which can be assigned to (1 1 1) and (2 0 0) crystal phases of metallic Ag (JCPDS file: 65-2871) [29]. Then, the diffraction peak of metallic Ag can be observed from the $Ag@AgCl/BiVO_4$ heterostructure, which suggested that certain amount of AgCl were obtained around the metallic Ag. While the diffraction peak of the AgCl was obviously detected at approximately (2θ) 32.2°, which can be assigned to (2 0 0) crystal phases corresponding to the diffractions of crystalline AgCl (JCPDS file: 31-1238) [30]. It provides sufficient evidence that the metallic Ag was not totally enwrapped by the AgCl in which act as the "linker" between $BiVO_4$ (0 4 0) and AgCl. Thus, the hierarchical Z-scheme photocatalyst of Ag@AgCl decorated on $BiVO_4$ (0 4 0) has been obtained. Fig. 2b and c are the typical TEM images of the pristine $BiVO_4$ and $Ag@AgCl/BiVO_4$ heterostructure. The inset of Fig. 2b shows a lattice spacing of 0.467 nm and 0.254 nm, corresponding to the interplanar spacing of (0 1 1) and (0 0 2) plane of $BiVO_4$ from HRTEM image, respectively [25,31]. It can be clearly seen that some particles located on the surface of the $Ag@AgCl/BiVO_4$ heterostructure. To investigate the local structure of materials, the Raman spectroscopy was employed to provide further evidence (Fig. 2d). The Raman vibrational bands at approximately 125.7, 210.4, 327.1, 366.0, 710.1 and 828.5 cm^{-1} were observed for pristine $BiVO_4$ which were in agreement with previous report [32]. As for $Ag@AgCl/BiVO_4$ heterostructure, the distinctive Raman bands related to the pristine $BiVO_4$ at 828.5 cm^{-1} assigned to the asymmetric and symmetric V–O stretching modes was shifted to 822.4 cm^{-1}, indicating that the local structures of $BiVO_4$ were to some extent changed [33]. Other vibrational peaks were related to the external vibration modes and asymmetric–symmetric bending vibrations of VO_4^{3-} at 125.7 cm^{-1}, 210.4 cm^{-1} and 327.1 cm^{-1}, 366.0 cm^{-1} respectively, which are well agreed with the pristine $BiVO_4$.

The UV–vis diffuse reflectance spectra (DRS) of the as-prepared materials are shown in Fig. 3 a. It can be clearly seen that almost all of the samples exhibit strong absorption in the visible light region except AgCl. Here, the photocatalyst of $Ag/BiVO_4$ exhibits a better light absorption than the others due to the more amount of loading metallic Ag^0 species on the crystal facet of $BiVO_4$ (0 4 0), which can be attributed to the surface plasmonic resonance (SPR) effect of Ag^0 NPs [34]. The absorbance of obtained $Ag@AgCl/BiVO_4$ heterostructure is between the pristine $BiVO_4$ and $Ag/BiVO_4$, which could be interpreted that some AgCl formed on the surface of Ag NPs and thus hindered the SPR-effect of Ag^0. Previous literature recorded that the capability of light absorption of photocatalyst is relative to evaluate the photocatalytic efficiency. However, it is worth pointing out that besides photoabsorption, other factors are also significant to realize the increasing photocatalytic efficiency of photocatalysts, such as the separation efficiency of photogenerated electron–hole pairs and the number of the effectively active sites for photocatalysis [35]. Clearly shown in Fig. 3b, the corresponding energy band gap of as-prepared $BiVO_4$ is around 2.4 eV, which is according to Kubelka–Munk band-gap estimation theory [7]. The

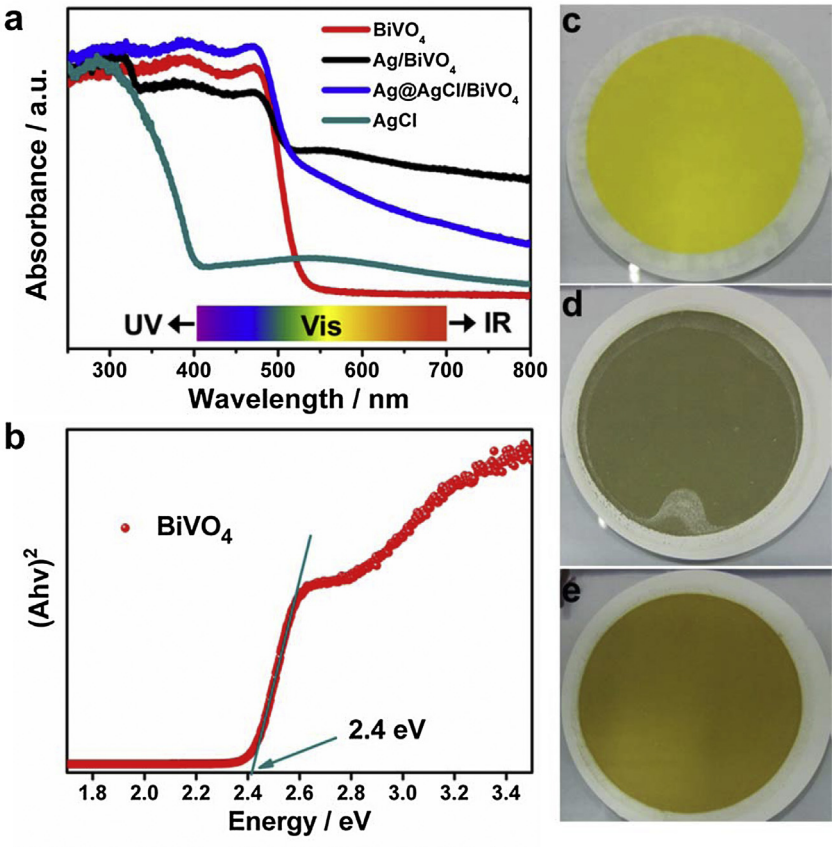

Fig. 3. The photophysical properties of the $BiVO_4$, $Ag/BiVO_4$, $Ag@AgCl/BiVO_4$ and AgCl materials. (a) UV–vis diffuse reflectance spectra of the $BiVO_4$, $Ag/BiVO_4$, $Ag@AgCl/BiVO_4$ and AgCl materials. (b) Energy band gap evaluation from the plots of $(Ah\nu)^{n/2}$ *vs.* the energy of the absorbed photon. (c–e) The digital photographs of the $BiVO_4$, $Ag/BiVO_4$ and $Ag@AgCl/BiVO_4$ in desiccation condition.

relative position of the conduction band edge can be calculated according to the following Eqs. (1) and (2) [36]:

$$E_{CB} = \chi - E_f - 0.5E_g \quad (1)$$

$$E_{VB} = E_{CB} + E_g \quad (2)$$

where χ is the absolute electronegativity of the semiconductor, which is defined as the geometric mean of the absolute electronegativity of the constituent atoms, and herein, it can be calculated by the arithmetic mean of the atomic electron affinity and the first ionization energy [37]. E_f is the energy of free electrons on the hydrogen scale (about 4.5 eV) [37]; E_g is the band gap of the semiconductor which can be obtained from Fig. 3b. Meanwhile, E_{CB} is the conduction band potential and E_{VB} is the valence band potential. Therefore, the band gap and the χ value of $BiVO_4$ are 2.4 eV and 6.04 eV, respectively. According to the above equations, the top of the VB position and the bottom of the CB position of $BiVO_4$ are calculated to be 2.74 and 0.34 eV, respectively. Fig. 3c–e are the typical digital photographs of the $BiVO_4$, $Ag/BiVO_4$ and $Ag@AgCl/BiVO_4$ photocatalyst samples in desiccation conditions.

X-ray photoelectron spectroscopy (XPS) was performed to further investigate the surface chemical composition and chemical states of the as-prepared samples (Fig. 4a–f). The survey XPS spectrum (Fig. 4a) of the as-prepared three samples confirmed the main ingredient elements of Ag and Cl, which agreed well with the results of elemental mapping analysis (Fig. 1f). Fig. 4b shows the Ag 3d spectrum of $Ag/BiVO_4$ and $Ag@AgCl/BiVO_4$. For $Ag@AgCl/BiVO_4$, the Ag 3d peak consists of two peaks at 367.2 and 373.2 eV, which are ascribed to Ag $3d_{5/2}$ and Ag $3d_{3/2}$, respectively. Furthermore, the peaks of Ag $3d_{5/2}$ and Ag $3d_{3/2}$ could be further divided into different peaks at 367.2 (Ag^+), 368.1 (Ag^0) as well as 373.2 (Ag^+), 374.1 eV (Ag^0), respectively [30]. The XPS results of Ag 3d confirm the existence of metallic Ag species and formation of the Ag@AgCl structure, which agree with the XRD analysis (Fig. 2a). The molar ratio of metallic Ag^0 species to total Ag was calculated to be 6.6% according to the XPS spectra (Fig. S2, in Supporting information). Yet for $Ag/BiVO_4$, it only has two peaks at approximately 368.1 and 374.1 eV, which could be attributed to the peaks of Ag $3d_{5/2}$ and Ag $3d_{3/2}$ of metallic Ag^0. As shown in Fig. 4c–e, the characteristic orbital of the Bi $4f_{7/2}$, Bi $4f_{5/2}$ peaks (Fig. 4c) and the V $2p_{3/2}$, V $2p_{1/2}$ peaks (Fig. 4e) of the $BiVO_4$, $Ag/BiVO_4$ and $Ag@AgCl/BiVO_4$ were observed with peak locations at 158.8, 164.1 and 517.0, 524.6 eV, respectively, which are closely corresponding to the Bi^{3+} and V^{5+} peaks in monoclinic scheelite $BiVO_4$ [38]. The peak at 530.2 eV can be ascribed to O 1s orbital of those three samples (Fig. 4d). For Cl 2p (Fig. 4f) of $Ag@AgCl/BiVO_4$ heterojunction photocatalyst, two peaks were obtained at binding energies of 197.2 and 198.7 eV, corresponding to Cl $2p_{3/2}$ and Cl $2p_{1/2}$, respectively. All the XPS binding energies coincide well with the reported literature.

3.3. Photoelectrochemical performance of photocatalysts

For the sake of evaluate the kinetics of charge transfer in this heterostructure composite, the electrochemical impedance spectroscopy (EIS) measurements were investigated [39]. As shown in Fig. 5a, the typical EIS Nyquist plots of $BiVO_4$, $Ag/BiVO_4$ and $Ag@AgCl/BiVO_4$ electrode were presented in the traditional three electrode system containing aqueous solution of mixed 5 mmol L^{-1} of $[Fe(CN)_6]^{3-/4-}$ and 1 mol L^{-1} of KCl electrolyte. The *x*-axis and *y*-axis represent the real part of the impedance (Z') and the negative number of the imaginary part of the impedance (Z''), respectively.

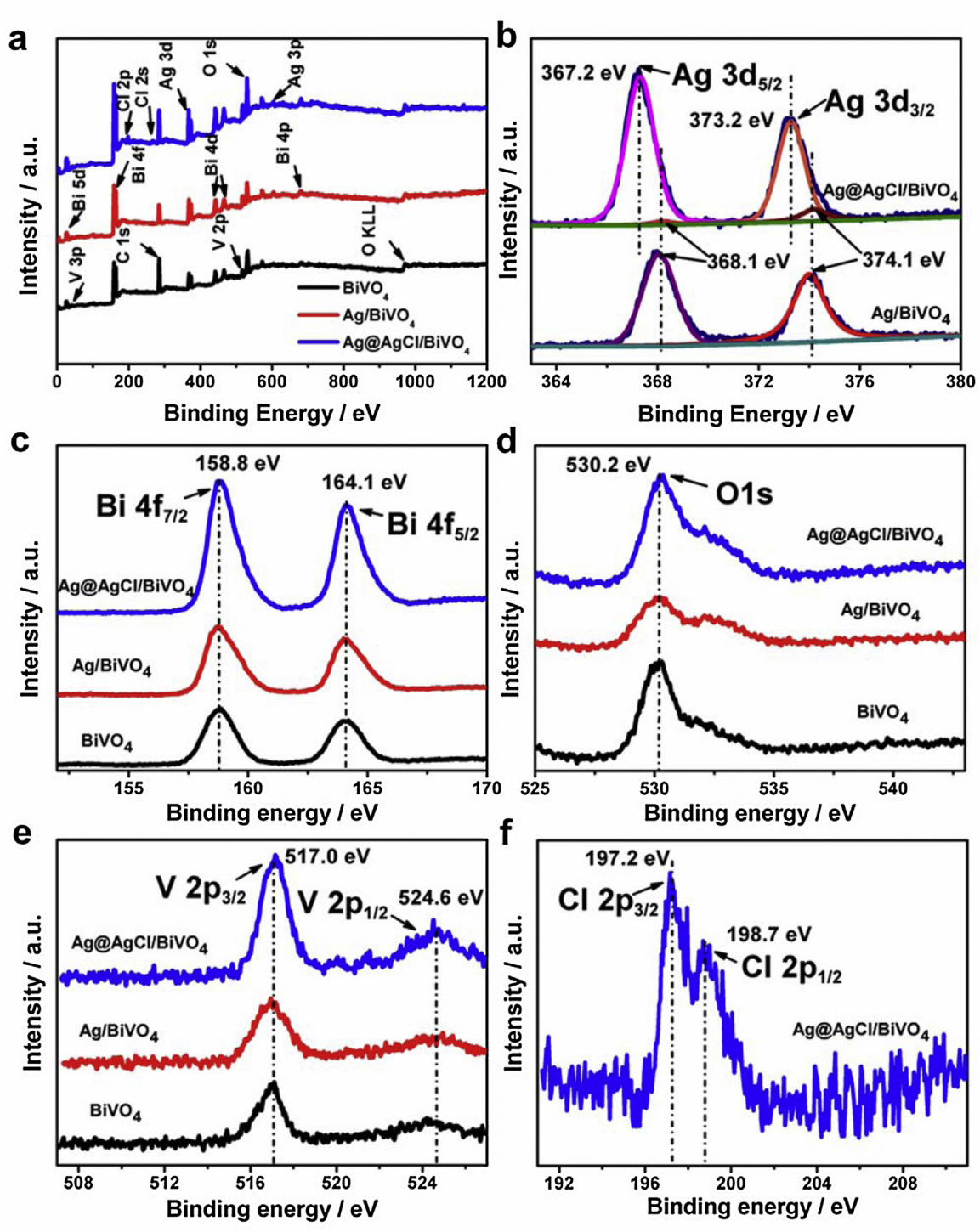

Fig. 4. XPS spectra of the as-prepared photocatalyst. (a) The survey XPS spectrum, (b) Ag 3d, (c) Bi 4f, (d) O 1s, (e) V 2p and (f) Cl 2p peaks related to the photocatalyst.

The Nyquist plot can be fitted in terms of the equivalent circuit (Randles–Ershler circuit model) as presented in the inset. Further, in this equivalent circuit, R_s, R_{ct} and CPE represent the solution resistance, charge transfer resistance across the interface of semiconductor||electrolyte and constant phase element for the semiconductor||electrolyte interface, respectively [40]. Clearly, it can be observed that the symbols indicate the experimental results tally with that of the lines fitting results by using an equivalent circuit from Fig. 5a. Thus, the semicircle radiuses in Fig. 5a are related to charge transfer at the interface of the semiconductor||electrolyte. The fitted values of R_{ct} were 115, 73 and 41 Ω for pristine $BiVO_4$, $Ag/BiVO_4$ and $Ag@AgCl/BiVO_4$, respectively. Previous studies have authenticated that efficient charge transfer at the semiconductor||electrolyte interface could suppresses the charge recombination and enhance the efficiency of photocatalytic process [38,40]. Since the fitted R_{ct} value of $Ag@AgCl/BiVO_4$ is about 3 times smaller than that of pristine $BiVO_4$, $Ag@AgCl/BiVO_4$ composite shows a preferable efficiency of charge transfer.

To investigate the photoresponses of the $BiVO_4$, $Ag/BiVO_4$ and $Ag@AgCl/BiVO_4$, the photocurrent transient response

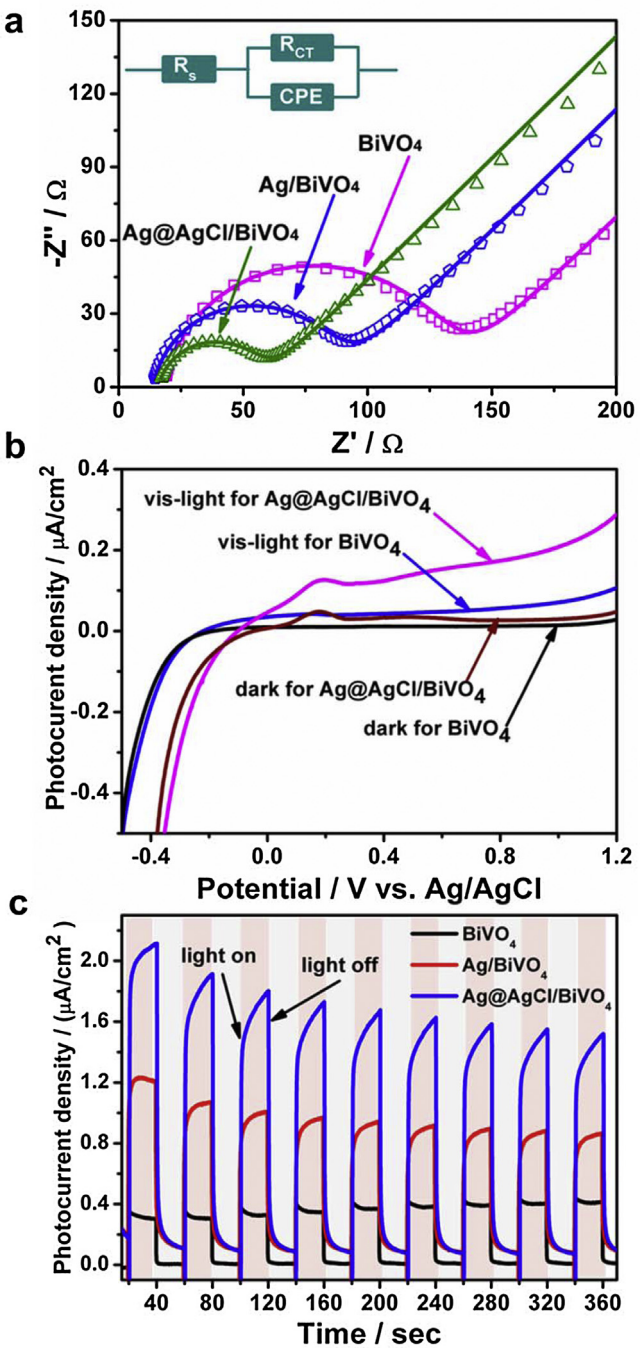

Fig. 5. (a) Electrochemical impedance spectroscopy Nyquist plots of $BiVO_4$, $Ag/BiVO_4$ and $Ag@AgCl/BiVO_4$. The solid line was fitted by ZSimpWin software using the proposed equivalent circuit model. The inset shows an ideal equivalent circuit for the working photoelectrode. (b) Time dependent photocurrent density of $BiVO_4$, $Ag/BiVO_4$ and $Ag@AgCl/BiVO_4$ at 0.2 V *vs.* Ag/AgCl. (c) Linear sweep voltammograms collected under visible light was eliminated by a 420 nm cutoff glass light filter. The scan rate: 10 mV s^{-1}.

measurement were carried out under illumination with several cycles of 20 s interval light on or off in Na_2SO_4 aqueous solutions. As shown in Fig. 5b, it demonstrates a clear comparison of the *I–t* curves for these three photocatalysts under visible light irradiation with the same wavelength range applied in the photocatalytic reactions. Conspicuously, the photocurrent value of the $Ag@AgCl/BiVO_4$ rapidly climbed up to a high current level when the light turned on and it presented a sharp decrease with the irradiation turned off. While it also return to a constant value when the light turned on again. Similar phenomena occurred upon $BiVO_4$ and $Ag/BiVO_4$ materials during the on–off irradiation process. However, it is worth noticing that the photocurrent density of the $Ag@AgCl/BiVO_4$ heterostructure electrode (*ca.* 1.52–2.12 μA cm^{-2}) is about 4–5 times higher than that of pristine $BiVO_4$ (*ca.* 0.30–0.40 μA cm^{-2}) and 2 times of $Ag/BiVO_4$ (*ca.* 0.80–1.20 μA cm^{-2}). Thus, such results can further validate that the as-prepared $Ag@AgCl/BiVO_4$ heterostructure performed higher separation efficiency of the photo induced electron–hole pairs and a relatively lower recombination rate under visible-light [31]. Owing to its excellent photo-electric reproducibility, such Z-scheme $Ag@AgCl/BiVO_4$ heterostructure will be sure to exhibit great potentials in the areas of photodetector, solar cell, water oxidation *etc.* [2,5,41].

An excellent material always accompany with many distinctive properties. Of course, the Z-scheme photocatalytic system of $Ag@AgCl/BiVO_4$ heterostructure is of no exception. Fig. 5c, herein, shows the linear sweep voltammograms (LSV) of $BiVO_4$ and $Ag@AgCl/BiVO_4$ heterostructure. The potential was linearly swept at a scan rate of 10 mV s^{-1} (*vs.* Ag/AgCl) in 0.5 M Na_2SO_4 electrolyte. The whole sweep process was implemented under visible light or dark conditions. The curves near zero current represent dark currents for these two photoctalysts. Obviously, the photocurrent of $Ag@AgCl/BiVO_4$ under vis-light is distinctly higher than that of $BiVO_4$ material, for the Z-scheme heterostructure could better facilitate the photo-induced carriers separation and suppress recombination of the electron–hole [41]. For $Ag@AgCl/BiVO_4$, the characteristic peaks at 0.2 V were observed when it was scanned under either the visible light or the dark, which should be the oxidation peaks of silver [42].

3.4. Evaluation of photocatalytic activity

To demonstrate the photocatalytic activity of such hierachical $Ag@AgCl/BiVO_4$ heterostructure photocatalyst, photocatalytic degradations of RhB dyestuff molecules by $BiVO_4$, $Ag/BiVO_4$ and $Ag@AgCl/BiVO_4$ heterostructure samples under visible-light irradiation were investigated as shown in Fig. 6. Current studies indicated that RhB dyestuff is the carcinogenic contaminant in potential. Thus, the effective conversion of toxic RhB dyestuff into the nontoxic small molecules would benefit both environment protection and human healthy. Fig. 6a displays photodegradation dynamic curves over aforementioned heterostructur photocatalysts. Compared with the pristine $BiVO_4$, $Ag@AgCl/BiVO_4$ exhibited a prodigious aggrandizement in degradation of RhB solution under visible light irradiation. It is observed that RhB has been fully decolorized after 35 min irradiation by employing $Ag@AgCl/BiVO_4$ heterostructure samples as photocatalyst, while only 0.4% and 42.4% of dyestuff solution was degraded over $BiVO_4$ and $Ag/BiVO_4$, respectively. Owing to the low concentration of the RhB solution (10 mg L^{-1}), the kinetics of the photocatalytic reactions were followed as a pseudo first order reaction [18,43], which can be expressed as: $\ln(C_0/C_t) = k_{app}t$. Here C_t is the concentration of RhB at irradiation time t, C_0 is the initial concentration of RhB. Then, k_{app} is the apparent reaction rate constant, which can be obtained from the slope of the liner correlation (Fig. 6b). Apparently, such $Ag@AgCl/BiVO_4$ heterostructure presents the highest k_{app} value of 0.12 min^{-1}, which is about 4 and 300 times higher than that of $Ag/BiVO_4$ (k_{app} = 0.03 min^{-1}) and pristine $BiVO_4$ (k_{app} = 0.0004 min^{-1}), respectively. The HPLC analysis further confirmed the photodegradation of RhB upon these photocatalysts (Fig. S3, in Supporting information). Moreover, the photoreaction dynamic curve of RhB in the presence of mechanical mixing with $BiVO_4$ and AgCl materials is shown in Fig. S4 (in Supporting information), which was also observed the lower photodegradation activity than the $Ag@AgCl/BiVO_4$ heterostructure. It provides sufficient evidence that the Z-scheme of $Ag@AgCl/BiVO_4$

heterostructure present excellent charge carries separation performance instead of mechanical mixing with two materials. Significantly, the stability and recyclability of Ag@AgCl/$BiVO_4$ heterostructure would also play the key role for practical applications. After a recycling application of four times, the catalytic efficiency of the Ag@AgCl/$BiVO_4$ heterostructure photocatalyst only has a little shrinkage which should be attributed to a small mass loss during the reclaim of photocatalyst in each recycling reaction process (Fig. S5, in Supporting information). Compared with the fresh heterostructure photocatalysts, the XRD analysis of Ag@AgCl/$BiVO_4$ after several times photocatalytic tests did not changed a lot (Fig. S6, in Supporting information), which further confirmed the remarkable reproducibility and long-term stability of such a Z-scheme photocatalyst. Moreover, to some extent, such a preferable photoactivity of Ag@AgCl/$BiVO_4$ heterostructure photocatalysts might also arise from its larger surface area (3.102 $m^2 g^{-1}$ for Ag@AgCl/$BiVO_4$ heterostructure, 2.831 $m^2 g^{-1}$ for Ag/$BiVO_4$ and 1.867 $m^2 g^{-1}$ for $BiVO_4$ materials, Fig. S7, in Supporting information).

3.5. Hypothesis of photocatalytic degradation mechanism

On the basis of characterization and photocatalytic data, it is confirmed that the dyestuffs of RhB can be successfully photodegradated upon the Ag@AgCl/$BiVO_4$ heterostructure photocatalyst in essence. Further, it is also crucial and necessary to propose and discuss the possible reaction mechanisms which are more beneficial for better understanding the enhancement in photocatalytic activity as well as the detailed degradation process (Fig. 7). Commonly, under visible-light irradiation, the photo-excited electrons and holes of pristine $BiVO_4$ will promptly recombine, which greatly hindered its further applications in photocatalysis [7,8]. AgCl cannot be excited under visible light irradiation due to its large band gap and the conduction band (CB) and valence band (VB) energy levels of AgCl are *ca.* −0.06 and 3.2 eV (*vs.* SHE), respectively [34]. In such a Z-scheme Ag@AgCl/$BiVO_4$ system, the $BiVO_4$ and metallic Ag^0 can successfully absorb visible-light photons to produce photogenerated electrons and holes under solar-light irradiation. Since a number of increased electrons will store in the lowest unoccupied orbital of Ag and thus lifted the Fermi energy level of Ag [44]. Afterwards, the superfluous electrons would migrate into the CB of the neighboring AgCl until the Fermi level of the Ag runs up to equilibrium again. The electrons will then transfer to the surface to react with oxygen to form $^{\bullet}O^{2-}$ active species ($(O^2/^{\bullet}O^{2-}) = -0.04$ eV *vs.* SHE) and further oxidize the organic pollutants [45–47]. Simultaneously, the photogenerated electrons in the conduction band of $BiVO_4$ will transfer to the Ag NPs to recombine with the photogenerated holes in the highest occupied orbital of Ag, while

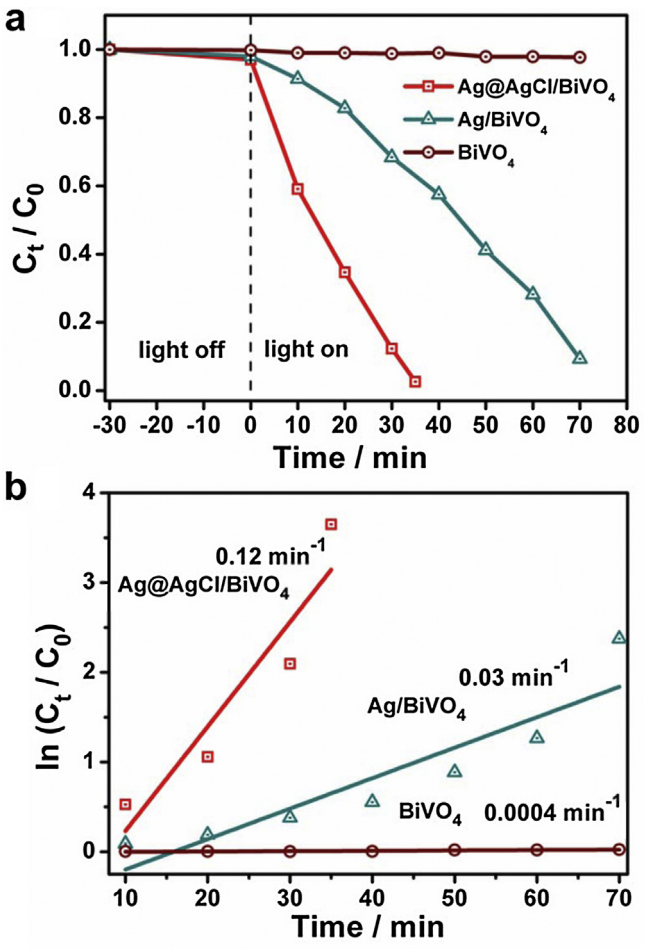

Fig. 6. (a) Photocatalytic degradation of RhB in the presence of different photocatalysts under visible-light irradiation. (b) ln (C_t/C_0) against reaction time for photodegradation of RhB over as-prepared photocatalysts. Normally, C_t stands for the concentration of RhB at time t, C_0 represents to the initial RhB concentration (10 mg L^{-1}).

the photo-excited holes of $BiVO_4$ remain on the VB to directly oxidize dye molecule or oxidize water molecule to form $^{\bullet}OH$ active species($(^{\bullet}OH/OH^-) = 1.99$ eV *vs.* SHE) [5,14,48]. Both the generated $^{\bullet}O^{2-}$ and $^{\bullet}OH$ active species can degradate organic pollutants into CO_2 and H_2O *etc.* In order to further validate the high photocatalytic activity mechanism of the Ag@AgCl/$BiVO_4$ heterostructure, the reactive species trapping experiments have also been performed [47]. As shown in Fig. S8 (in Supporting information),

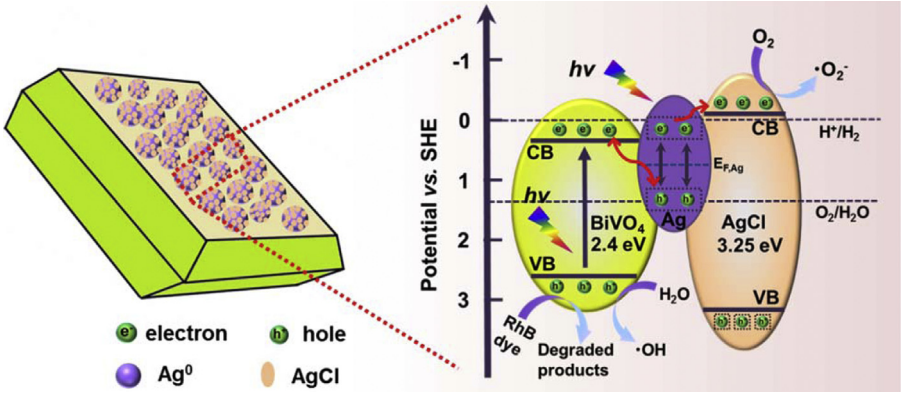

Fig. 7. The schematic diagram illustration of Ag@AgCl decorated on the (0 4 0) crystal facet of $BiVO_4$ and the proposed Z-scheme mechanism photodegradation of RhB dye over Ag@AgCl/$BiVO_4$ heterostructure photocatalyst under visible light irradiation.

it can be clearly seen that the EDTA (h^+ scavenger) and BZQ ($^{\bullet}O^{2-}$ radical scavenger) caused fast deactivation of the Ag@AgCl/$BiVO_4$ heterostructure photocatalyst and retarded the reaction rate. It demonstrated that the photo-induced h^+ and $^{\bullet}O^{2-}$ radical are the predominant active species in this photocatalytic system. Yet only a weak inhibition was observed on the photo-decoloration of RhB when TBA ($^{\bullet}$OH radical scavenger) was introduced into this photocatalytic system, which indicated that the $^{\bullet}$OH radical plays a minor role to photocatalytic reaction.

Consequently, such distinctive heterogeneous Z-scheme photocatalytic system overcomes the drawbacks of single-component $BiVO_4$ or AgCl and realizes the high charge-separation efficiency and strong redox ability as well as long-term stability. It is especially noteworthy that the Ag NPs not only act as the electron mediator, but also can absorb the photons from incident light and demonstrate the SPR-effect. Moreover, the aggregation of photogenerated electrons in the CB of AgCl makes AgCl an electron-rich region, which can suppress the photo-oxidation of AgCl. Similarly, the aggregation of photogenerated holes in the VB of $BiVO_4$ makes $BiVO_4$ a rich-hole region, which can protect $BiVO_4$ from the photoreduction.

4. Conclusions

In summary, the Ag@AgCl core–shell structure decorated on (040) crystal facet of $BiVO_4$ as a hierarchical Z-scheme photocatalytic system has been successfully constructed by means of reduction and oxidation route. Further, such Ag@AgCl/$BiVO_4$ heterostructure showed highly efficient photocatalytic performance for RhB degradation under visible light irradiation. Such excellent performance should be attributed to the Z-scheme system, which can improve the photo-induced carriers separation efficiency and benefit to suppress recombination of the electron–holes, as well as leaving more charge carriers to form reactive species. In this hybridization system, the metallic Ag species can both act as the solid state electron mediator and enhance the visible light absorption corresponding with SPR-effect. It is expected that this class of $BiVO_4$-based all-solid-state Z-scheme photocatalysts will provide a novel perspective for understanding the mechanism of interfacial charge transfer. What is more, we anticipate this work may open up new insights into the architectural design of novel Z-scheme photocatalysts with high photoactivity and further utilization in the field of environmental or energy.

Acknowledgements

The authors are most grateful to the NSFC, China (Nos. 21205112, 21225524, 21475122 and 21127006), the Department of Science and Techniques of Jilin Province (Nos. 20120308, 201215091 and SYHZ0006) and Chinese Academy of Sciences (Nos. YZ201354 and YZ201355) for their financial support.

Appendix A. Supplementary data

Supplementary data associated with this article can be found, in the online version, at http://dx.doi.org/10.1016/j.apcatb.2015.01.043.

References

[1] S.Y. Reece, J.A. Hamel, K. Sung, T.D. Jarvi, A.J. Esswein, J.J. Pijpers, D.G. Nocera, Science 334 (2011) 645–648.
[2] A. Kudo, Y. Miseki, Chem. Soc. Rev. 38 (2009) 253–278.
[3] H. Kisch, Angew. Chem. 52 (2013) 812–847.
[4] H. Wang, L. Zhang, Z. Chen, J. Hu, S. Li, Z. Wang, J. Liu, X. Wang, Chem. Soc. Rev. 43 (2014) 5234–5244.
[5] P. Zhou, J. Yu, M. Jaroniec, Adv. Mater. 26 (2014) 4920–4935.
[6] Y.P. Xie, Z.B. Yu, G. Liu, X.L. Ma, H.-M. Cheng, Energy Environ. Sci. 7 (2014) 1895–1901.
[7] W.J. Jo, J.-W. Jang, K.-j. Kong, H.J. Kang, J.Y. Kim, H. Jun, K.P.S. Parmar, J.S. Lee, Angew. Chem. Int. Ed. 51 (2012) 3147–3151.
[8] M. Xie, X. Fu, L. Jing, P. Luan, Y. Feng, H. Fu, Adv. Energy Mater. 4 (2014), http://dx.doi.org/10.1002/aenm.201300995.
[9] Q. Wang, J. Li, Y. Bai, J. Lian, H. Huang, Z. Li, Z. Lei, W. Shangguan, Green Chem. 16 (2014) 2728–2735.
[10] C. Li, P. Zhang, R. Lv, J. Lu, T. Wang, S. Wang, H. Wang, J. Gong, Small 9 (2013) 3951–3956.
[11] H. Tada, T. Mitsui, T. Kiyonaga, T. Akita, K. Tanaka, Nat. Mater. 5 (2006) 782–786.
[12] K. Sekizawa, K. Maeda, K. Domen, K. Koike, O. Ishitani, J. Am. Chem. Soc. 135 (2013) 4596–4599.
[13] X. Wang, S. Li, Y. Ma, H. Yu, J. Yu, J. Phys. Chem. C 115 (2011) 14648–14655.
[14] A. Iwase, Y.H. Ng, Y. Ishiguro, A. Kudo, R. Amal, J. Am. Chem. Soc. 133 (2011) 11054–11057.
[15] C. Li, S. Wang, T. Wang, Y. Wei, P. Zhang, J. Gong, Small 10 (2014) 2783–2790.
[16] Q. Jia, A. Iwase, A. Kudo, Chem. Sci. 5 (2014) 1513.
[17] R. Li, F. Zhang, D. Wang, J. Yang, M. Li, J. Zhu, X. Zhou, H. Han, C. Li, Nat. Commun. 4 (2013) 1432.
[18] R. Li, H. Han, F. Zhang, D. Wang, C. Li, Energy Environ. Sci. 7 (2014) 1369.
[19] G. Xi, J. Ye, Chem. Commun. 46 (2010) 1893–1895.
[20] H. Li, T. Wu, B. Cai, W. Ma, Y. Sun, S. Gan, D. Han, L. Niu, Appl. Catal. B: Environ. 164 (2015) 344–351.
[21] B. Cai, J. Wang, D. Han, S. Gan, Q. Zhang, Z. Wu, L. Niu, Nanoscale 5 (2013) 10989–10995.
[22] J. Sun, G. Chen, J. Wu, H. Dong, G. Xiong, Appl. Catal. B: Environ. 132 (2013) 304–314.
[23] J. Yu, A. Kudo, Adv. Funct. Mater. 16 (2006) 2163–2169.
[24] A.Y. Booshehri, S. Chun-Kiat Goh, J. Hong, R. Jiang, R. Xu, J. Mater. Chem. A 2 (2014) 6209.
[25] D. Wang, H. Jiang, X. Zong, Q. Xu, Y. Ma, G. Li, C. Li, Chemistry 17 (2011) 1275–1282.
[26] S. Weng, B. Chen, L. Xie, Z. Zheng, P. Liu, J. Mater. Chem. A 1 (2013) 3068.
[27] B. Ma, J. Guo, W.-L. Dai, K. Fan, Appl. Catal. B: Environ. 130–131 (2013) 257–263.
[28] T.W. Kim, K.S. Choi, Science 343 (2014) 990–994.
[29] M. Zhu, P. Chen, M. Liu, ACS Nano 5 (2011) 4529–4536.
[30] Y. Tang, Z. Jiang, G. Xing, A. Li, P.D. Kanhere, Y. Zhang, T.C. Sum, S. Li, X. Chen, Z. Dong, Z. Chen, Adv. Funct. Mater. 23 (2013) 2932–2940.
[31] X. Gao, H.B. Wu, L. Zheng, Y. Zhong, Y. Hu, X.W.D. Lou, Angew. Chem. Int. Ed. 126 (2014) 6027–6031.
[32] N. Wetchakun, S. Chaiwichain, B. Inceesungvorn, K. Pingmuang, S. Phanichphant, A.I. Minett, J. Chen, ACS Appl. Mater. Interfaces 4 (2012) 3718–3723.
[33] J.K. Cooper, S. Gul, F.M. Toma, L. Chen, P.-A. Glans, J. Guo, J.W. Ager, J. Yano, I.D. Sharp, Chem. Mater. 26 (2014) 5365–5373.
[34] D. Chen, T. Li, Q. Chen, J. Gao, B. Fan, J. Li, X. Li, R. Zhang, J. Sun, L. Gao, Nanoscale 4 (2012) 5431–5439.
[35] P.M. Rao, L. Cai, C. Liu, I.S. Cho, C.H. Lee, J.M. Weisse, P. Yang, X. Zheng, Nano Lett. 14 (2014) 1099–1105.
[36] M.L. Guan, D.K. Ma, S.W. Hu, Y.J. Chen, S.M. Huang, Inorg. Chem. 50 (2011) 800–805.
[37] Z. Lou, B. Huang, Z. Wang, X. Ma, R. Zhang, X. Zhang, X. Qin, Y. Dai, M.-H. Whangbo, Chem. Mater. 26 (2014) 3873–3875.
[38] K.P. Parmar, H.J. Kang, A. Bist, P. Dua, J.S. Jang, J.S. Lee, ChemSusChem 5 (2012) 1926–1934.
[39] M. Zhou, H.B. Wu, J. Bao, L. Liang, X.W. Lou, Y. Xie, Angew. Chem. 52 (2013) 8579–8583.
[40] S.J. Hong, S. Lee, J.S. Jang, J.S. Lee, Energy Environ. Sci. 4 (2011) 1781.
[41] D. Eisenberg, H.S. Ahn, A.J. Bard, J. Am. Chem. Soc. 136 (2014) 14011–14014.
[42] D.A. Slanac, W.G. Hardin, K.P. Johnston, K.J. Stevenson, J. Am. Chem. Soc. 134 (2012) 9812–9819.
[43] S. Han, L. Hu, N. Gao, A.A. Al-Ghamdi, X. Fang, Adv. Funct. Mater. 24 (2014) 3725–3733.
[44] J.W. Ha, T.P. Ruberu, R. Han, B. Dong, J. Vela, N. Fang, J. Am. Chem. Soc. 136 (2014) 1398–1408.
[45] Z. Zhang, J.T. Yates Jr., Chem. Rev. 112 (2012) 5520–5551.
[46] K. Maeda, ACS Catal. 3 (2013) 1486–1503.
[47] L. Ye, J. Liu, C. Gong, L. Tian, T. Peng, L. Zan, ACS Catal. 2 (2012) 1677–1683.
[48] Q. Wang, T. Hisatomi, S.S.K. Ma, Y. Li, K. Domen, Chem. Mater. 26 (2014) 4144–4150.